Electrochimica Acta 464 (2023) 142946

Contents lists available at ScienceDirect

Electrochimica Acta

journal homepage: www.journals.elsevier.com/electrochimica-acta

Enhanced ORR activity of S- and N-modified non-noble metal-doped carbons with bamboo-like C nanotubes grafted onto their surface

Erlind Mysliu [a,1], Marco Scavini [a], Saveria Santangelo [b,c,*], Salvatore Patanè [c,d], Nicoletta Ditaranto [e], Paola Bassani [f], Mariangela Longhi [a,*]

[a] Università degli Studi di Milano, Dipartimento di Chimica, Via Golgi 19, 20133 Milano
[b] Università "Mediterranea", Dipartimento di Ingegneria Civile, dell'Energia, dell'Ambiente e dei Materiali (DICEAM), Via Zehender, Loc. Feo di Vito, 89122 Reggio Calabria, Italy
[c] National Reference Center for Electrochemical Energy Storage (GISEL), Consorzio Interuniversitario Nazionale per la Scienza e Tecnologia dei Materiali (INSTM), 50121 Firenze, Italy
[d] Università degli Studi di Messina, Dipartimento di Scienze Matematiche e Informatiche, Scienze Fisiche e Scienze della Terra (MIFT), Viale Stagno d'Alcontres 31, 98166 Messina, Italy
[e] Università degli Studi di Bari Aldo Moro, Dipartimento di Chimica, Via Orabona 4, 70125 Bari, Italy. CSGI - Centre for Colloid and Surface Science, Bari Unit
[f] Consiglio Nazionale delle Ricerche – Istituto per la Chimica della Materia Condensata e di Tecnologie per l'Energia, Via Previati 1/E, 23900 Lecco, Italy

ARTICLE INFO

Keywords (max 6):
ORR
Pt-free carbon electrocatalysts
N- and S- modified carbons
carbons bearing CNTs
metal-doped carbons

ABSTRACT

Discovering low-cost and earth-abundant electrocatalysts for oxygen reduction reaction (ORR) is essential for advanced energy conversion technologies. A large set of carbon-based ORR electrocatalysts was prepared by a two-step pyrolysis at 600 °C and then at 900 °C. Gelling sugar, guanidine acetate and cysteine were used as carbon, nitrogen and sulphur sources, respectively; iron and copper salts were utilised to produce non-noble metal-doped carbons. Silica was used as templating agent. The produced materials were thoroughly characterized by means of BET, XPS, XRPD and micro-Raman spectroscopy to investigate their physicochemical properties, and by means of RDE and RRDE methods to study their electrocatalytical properties towards ORR. They consist in sulphur- and/or nitrogen-modified carbons, some of which iron- and/or copper-doped. The massive carbonaceous structure bears bamboo-like C nanotubes onto the surface of iron-containing electrocatalysts. The best ORR electrocatalytic performance pertains to S- and N-modified carbons bearing nanotubes, which points to the occurrence of synergistic effects between heteroatoms and active sites associated to the presence of nanotubes.

1. Introduction

In September 2015, 193 Member Countries of the United Nations signed the 2030 Agenda. In this historical document, approved by UN General Assembly, 17 Sustainable Development Goals to be achieved by 2030 were set. The seventh goal is "Affordable and Clean Energy", *i.e.* guaranteeing everyone access to an economical, reliable, sustainable and modern energy system [1].

Electrochemical systems represent good candidates to reach this goal, both as energy storage systems, *e.g.* fuel cells and zinc-air battery, and conversion systems, *e.g.* supercapacitors [2–4]. In the former, the reduction reaction represents the most challenging aspect since the oxygen reduction reaction (ORR) is characterized by a sluggish kinetic, which limits the energy-conversion efficiency [5,6] and needs an efficient electrocatalyst. Platinum is the most used material, but it has high costs, limited availability, and technological limitations, as Ostwald ripening and coalescence [7]. The worldwide research to replace Pt with a platinum group metal free material with relatively similar efficiency, higher stability, but lower costs started in the sixties with the seminal work of Jasinsky on metal phthalocyanines [8]. Since then, many articles about metal-doped nitrogen-modified carbon-based materials have been published [9–11]. The presence of an element as nitrogen, having an electronegativity higher than carbon, induces a modification of the electronic structure of nearest neighbour C atoms with an asymmetric redistribution of their charge and/or spin densities with their activation [12]. This point defect, associated with other intrinsic structural defects,

* Corresponding authors.
E-mail addresses: saveria.santangelo@unirc.it (S. Santangelo), mariangela.longhi@unimi.it (M. Longhi).
[1] Present Address: Norwegian University of Science and Technology, NTNU, Department of Materials Science and Engineering, Kjemi 2, 430 Gløshaugen, Norway.

https://doi.org/10.1016/j.electacta.2023.142946
Received 1 May 2023; Received in revised form 21 July 2023; Accepted 26 July 2023
Available online 30 July 2023

as topological defects, edges, vacancies/holes, distortion, and curvature has therefore an important role in increasing electrocatalytic properties of carbon materials, with a consequent improvement of ORR activity [12–15]. Furthermore, the introduction of iron further boosts this activity [16]. Many studies have been done to find real active sites on these materials, and some authoritative groups have demonstrated that they are based on Fe-N_x sites incorporated in graphene planes of carbon [17,18], since these clusters would promote oxygen adsorption and, therefore, the breaking of bond between the two oxygen in this molecule [16].

Nevertheless, in the last decade, modification with single heteroatoms different from N (*e.g.* P, B, S) has been considered [19,20], because the presence of these heteroatoms, as in the case of nitrogen, tunes the bandgap and modifies the surface electronic behaviour, enhancing the electrochemical activity [19,20]. However, recent studies have evidenced that the modification with two different heteroatoms induces a synergistic effect with an improvement of electrocatalytic activity compared to the performance obtained by a single-doped material [21]. This experimental evidence is also supported by density functional theory (DFT) calculations, which show that single heteroatom doping induces less positive and negative charges on neighbouring C atoms than that generated by co-doping [20]. One of the most promising elements to enhance the electrocatalytic property of carbon is sulphur [20]. This element, while having an electronegativity similar to C, has an atomic radius larger (102 pm) than carbon (70 pm) and nitrogen (65 pm) [22]. Therefore, its insertion in graphene plane generates strain and, consequently, structural defects that can provide active sites for ORR [23]. Moreover, as previously observed, the presence of S in the graphene planes leads to a contemporary variation of energy levels of S and C with a non-uniformity of spin density distribution [24], and, thanks to the large S lone pairs, a rising of polarizability that favours the interaction with oxygen [25]. Finally, sulphur can be present in carbon matrix as -C-S-C- or -C-SO_x, and these two S-species possess higher spin densities, that induces high capacitance and a boosting of adsorption and breaking bond of O_2 [20,26].

Further metal doping of these electrocatalysts improves their electrochemical activity, especially in the case of iron, as shown in [27]. Moreover, it has been demonstrated that also in these electrocatalysts the major contributor to ORR is the Fe-N_x cluster [27].

Notwithstanding the aforesaid advantages in terms of electrocatalytic activity, the introduction of S in a carbon matrix could generate such excessive strain to provoke the structure destruction. Therefore, a trade-off between density of the active sites and electrochemical activity is necessary [28]. The use of carbon nanostructures could be a solution of this problem, and the proposal of electrocatalysts based on graphene, and on S-N doped CNTs could be intriguing. In particular, results on S-N doped CNTs are promising [29], but, unfortunately, the production yield of this type of materials is not so high.

In order to overcome this last aspect, to take advantage of the specificities of S-N doped materials and so on to obtain the best electrocatalyst in terms of efficiency, chemical and mechanical stability in high yield with a facile synthesis, the combination of good properties of both metal S-N doped carbon and S-N doped CNTs in an unique material, *i.e.* an activated carbon S-N doped and covered by CNTs, seems very challenging, but apparently not easily accessible. However, in [30,31], it has been shown that by a simple synthesis path it is possible to obtain good yield electrocatalysts, very active toward ORR based on metal doped N-modified active carbons, with N-doped CNTs grafted onto their surface [30]. Therefore, by using appropriate precautions, obtaining a material possessing all the best behaviour cited above should not be a chimera.

In this work, we demonstrate that i) S- and N-modified Me-doped C materials bearing on surface CNTs can be obtained by a facile synthesis route and ii) the presence of nanotubes is necessary to have electrocatalysts with a high activity toward ORR.

2. Experimental

2.1. Reagents

All reagents were purchased from Sigma-Aldrich/Merck and used without further purification: iron (II) acetate (95%), copper (II) acetate (99.999% trace metal bases), guanidine acetate ($CH_5N_3{\cdot}CH_3COOH$), L-cysteine ((*R*)−2-Amino-3-mercaptopropionic acid, >98%) and silica gel 60 (0.063–0–200 mm, 70–230 mesh ASTM). Gelling sugar (Südzucher AG, Mannheim, Germany) containing sucrose:pectin = 98%:2% [30]. A Pt-based commercial electrocatalyst, EC-20 (ElectroChem, Inc., nominal Pt loading 20%), was analysed and used as a reference material.

2.2. Synthesis procedure

The synthesis path was previously reported [30,31]. In brief, gelling sugar (3 g), heteroatom precursor (a total amount of 0.0168 mol of guanidine acetate or cysteine or a equimolar mixture of them, 0.0084:0.0084, if used together) and metal (Me) acetate (1 wt.% total metal ion calculated on the total mass of sugar and heteroatom precursor, Me = Fe, Cu, or a Fe:Cu = 0.5 wt.%:0.5 wt.% mixture) were added to silica powder (4.3 g) and mixed in a mortar. For an easier identification of the samples their code summarises the precursors utilised for the synthesis, namely sugar (Z), guanidine acetate (G) and/or cysteine (C), and the metal dopant (if any), as reported in Table 1.

This mixture was carbonized in a first heating step in a vertical furnace (ramp = 6 °C min^{-1}, T = 600 °C, 1 h, N_2 flow rate = 100 cm^3 min^{-1}, cooling down under nitrogen flux outside the furnace) followed by lixiviation in boiling NaOH (3 mol dm^{-3}, 3 h) to remove silica. After washing, the carbon was dried (T = 110 °C, 24 h, N_2) and, finally, calcinated (ramp= 6 °C min^{-1}, T = 900 °C, 3 h, N_2 flow rate = 100 cm^3 min^{-1}, cooling down under nitrogen flux outside the furnace).

For the sake of comparison, samples containing heteroatoms and metals have been also prepared without using sugar. In this case, yield was lower, and the formation of finer powder during carbonization caused occlusion and blocking of gas tubes. For safety reasons, these samples were no longer considered.

2.3. Methods

Specific surface area and porosity distribution were obtained from N_2 adsorption/desorption isotherms at 77 K using a Micromeritics Tristar II 3020 (Micromeritics) apparatus and the instrumental software (Version 1.03) and applying Brunauer–Emmett–Teller (BET) and Barrett–Joyner–Halenda analyses, respectively. Sample powders were heat-treated (T = 150 °C, 4 h, N_2) before the analysis to remove adsorbed water. Porosity distribution was determined by analysing the adsorption nitrogen isotherm branch, since in the presence of hysteresis, it corresponds to a more stable thermodynamic condition [32].

The pyrolysis of the samples was ascertained using Micro-Raman

Table 1
Description of synthesized sample.

Sample Name	Sugar (Z)	Cysteine (C)	Guanidine Acetate (G)	Iron Acetate (Fe) /%	Copper Acetate (Cu) /%
ZC	×	×	–	–	–
ZG	×	–	×	–	–
ZCG	×	×	×	–	–
ZCFe	×	×	–	1.00	–
ZGFe	×	–	×	1.00	–
ZCGFe	×	×	×	1.00	–
ZCGCu	×	×	×	–	1.00
ZCFeCu	×	×	–	0.50	0.50
ZGFeCu	×	–	×	0.50	0.50
ZCGFeCu	×	×	×	0.50	0.50

× denotes the presence of a specific compound in the precursor mixture.

spectroscopy (MRS). Raman scattering excited by a solid-state laser operating at 2.33 eV (532 nm) was measured by using a NTEGRA - Spectra SPM spectrometer (NT-MDT LLC, Moscow, Russia), equipped with MS3504i 350-mm monochromator and ANDOR Idus CCD (Oxford Instruments, Belfast, United Kingdom). The scattered light from the sample was collected by a Mitutoyo 0.75 numerical aperture 100X objective. The use of a very low laser power (250 μW at the sample surface) prevented local heating of the samples and annealing effects.

X-ray Photoelectron Spectroscopy (XPS) analyses were run on a PHI 5000 Versa Probe II Scanning XPS Microprobe spectrometer (ULVAC-PHI Inc., Kanagawa, Japan). Measurements were done with a monochromatic Al Kα source (X-ray spot 100 μm) at a power of 24.8 W. Wide scans and detailed spectra were acquired in Fixed analyzer Transmission (FAT) mode with a pass energy of 117.40 eV and 29.35 eV, respectively. An electron gun was used for charge compensation (1.0 V 20.0 μA). Data processing was performed by using the MultiPak software v. 9.5.0.8 (ULVAC-PHI Inc., Kanagawa, Japan).

X-ray Powder Diffraction (XRPD) measurements were carried on lanthanum hexaboride (NIST 660c) standard, and graphite (Aldrich, product number: 282,863) as reference sample, and on most of the samples (ZC, ZG, ZCG, ZCFe, ZGFe, ZCGFe, ZCGCu, and ZCGFeCu). Samples were placed in kapton® capillaries (diameter 1 mm) and measured at the Powder Diffraction and Total scattering beamline P02.1 of PETRA III Synchrotron in Hamburg (D) using a wavelength λ = 0.20735 Å and a Varex XRD 4343CT area detector. 30 frames were collected on each sample. The area detector was placed at a distance of 280 mm with the beam near a corner of the detector to reach a maximum Q (= $4\pi\sin(\theta_{max})/\lambda$) value as large as ≈28.25 $Å^{-1}$, using a quarter Debye-Sherrer ring). The pattern collected on a LaB6 standard was used to perform the detector calibration. Following frames merging, azimuthal integration to transform 2D data into 1D ones (I *vs* 2θ) was performed using Fit2D [33]

Data in the reciprocal space were employed for crystalline phases identification using Match! (version 2.4.7) [34] and for Rietveld analysis. Considering the complexity of the Me-S phase diagram (Me= Fe, Cu), and the fact that the angular resolution of the experiment does not allow to discriminate amongst phases with small symmetry differences amongst each other, in the attribution of phases the highest symmetry phase amongst the possible ones was selected.

The structural models were fitted using GSAS [35] up to a maximum momentum transfer value $Q_{max} = 4\pi\sin\theta/\lambda = 10.5$ $Å^{-1}$.

The XRPD data were Fast Fourier Transformed after suitable corrections and normalization to get the Pair Distribution Functions PDF/G (r) functions as described in the literature [36] using the program PDFGetX3 [37]. Maximum value of Q used for PDF calculation was Q_{max} = 23 $Å^{-1}$. PDF analysis was carried out using both direct analysis of the diffraction peaks [38,39] and fitting the pair distribution functions G(r) against structural models using the so-called Real Space Rietveld Analysis (RSRA) as implemented in PDFgui [40]. The instrumental contribution to G(r) dampening was calculated fitting the G(r) function of LaB6 sample in the 1–100 Å interval using RSRA, obtaining Q_{damp}=0.0303.

Scanning Electron Microscopy (SEM) investigations were performed with a Field Emission Gun SEM SU70 (Hitachi, Japan), operated with normal mode and 10 kV acceleration voltage. Secondary Electron (SE) and Back Scattered Electron (BSE) detectors were used, in order to get information on general morphology and metals distribution. Observations were performed on small quantities of the specimens, that were placed on reference carbon tape, and then sputter coated with gold. Features were also analysed by Energy-Dispersive X-ray analysis (EDX), with UltraDry silicon drift X-ray detector (Thermo Fisher Scientific, USA). Additionally, a small quantity of ZCGFeCu specimen was dispersed in ethanol, then let dry on a Formvar coated copper grid (Agar scientific), and observed with Transmission Electron (TE) detector, under an acceleration voltage of 25 kV.

Cyclic Voltammetry (CV) results were obtained by an Amel potentiostat (Mod. 7050) in 0.1 mol dm^{-3} KOH at 25 °C using a single-compartment cell. A glassy carbon of a Rotating Disk Electrode, RDE, (EDI, Tacussel; geometric area = 0.07 cm^2) was used as working electrode, with a (Ag/AgCl) reference electrode in 3 mol dm^{-3} NaCl (+0.971 vs RHE/V, $\gamma_{\pm,KOH}$=0.798 [41]), separated from the cell by a closed salt bridge filled with 0.1 mol dm^{-3} KOH, and a pyrolytic graphite as counter electrode. An additional Rotating Ring Disk Electrode, RRDE, (Pine Instrument Co., Collection Efficiency = 0.235, geometric area = 0.196 cm^2, ring: Pt) was used with an Autolab Bipotentiostat to measure the hydrogen peroxide yield and the number of exchanged electrons. Inks for the loading of electrode were obtained by suspending an activated carbon sample (10 mg) in a mixture of 1 mL H_2O and 5 μL Nafion®. After 10 min sonication, the suspension was ball-milled for 20 min at 10 Hz in an agate jar (Retsch MM400). At the end, an aliquot of this mixture was pipetted onto the electrode tip and dried under a tungsten lamp (7 μL for RDE and 20 μL for RRDE). The catalyst amount on both electrodes was 1 mg cm^{-2}. Prior to O_2 reduction, the working electrode was left equilibrating 20 min in the solution, flushed with O_2. Then, a conditioning step in O_2 was performed (100 min, $\nu = 5$ mV s^{-1}, $\omega = 0$ rpm) at the end of which CVs were recorded at ν = 5 mV s^{-1} and at various electrode rotation rates. To check electrode stability and internal reproducibility several CVs at = 1600 rpm were recorded in each run. Finally, the cell was flushed with N_2 to record the intrinsic currents of the materials. Subtracting these results from the corresponding ones obtained in O_2, a background correction was obtained. In any case each CV measurement consisted of three continuous cycles between +1.120 vs RHE/V and + 0.070 vs RHE/V, starting at + 1.120 vs RHE/V through + 0.070 and ending at + 1.120 vs RHE/V. Data reported in tables and plots were obtained on the reduction part of the third cycle. In RRDE measurements ring potential was set to 1.31 vs RHE/V.

Oxygen Reduction Onset potential was calculated by applying the tangent method to the "knee" of the curve at low overpotentials. The number of exchanged electrons for all samples was calculated by averaging values obtained applying eq. (1) on RRDE results [42] in the range of diffusion limiting current.

$$n = 4 \times \frac{I_D}{I_D + \frac{I_R}{N}} \quad (1)$$

where I_R, I_D and N are the ring current, the disk current at a specific potential E, and ring collection efficiency (0.235), respectively.

Considering the reduction branch of CV results of RDE, Tafel slopes for ORR were determined by eq. (2) plotting the calculated overpotential η *vs* j_k, the current density in the absence of any mass-transfer effects.

$$\eta = \frac{RT}{\alpha F} ln(j_0) - \frac{RT}{\alpha F} ln(j_k) \quad (2)$$

where R, T and F have the usual meaning, α is the charge transfer coefficient, j_0 is the exchange current density.

j_k was determined by reporting current density data in Koutecky-Levich coordinates (j^{-1} vs $\omega^{-1/2}$) at various potentials (Eq. (3) [31], which had been employed to calculate overpotentials.

$$\frac{1}{j} = \frac{1}{j_k} + \frac{1}{j_l} \quad (3)$$

where j_l=$0.62nFD^{2/3}\nu^{-1/6}C\omega^{1/2}$, with n the number of exchanged electrons, F the Faraday constant, D the diffusion coefficient of O_2 (1.67×10^{-5} cm^2 s^{-1} in 0.1 mol dm^{-3} KOH [31]), ν the kinematic viscosity of the electrolyte (0.01 cm^2 s^{-1} in 0.1 mol dm^{-3} KOH [31]), ω the angular frequency of rotation (rad s^{-1}), k the electron transfer rate constant, and finally C the solution concentration of reactant (C = 1.38 mol cm^{-3} for O_2-saturated 0.1 mol dm^{-3} KOH [31]).

Hydrogen peroxide yield was calculated by Eq. (4) [43], where I_R, I_D and N are the ring current, the disk current at a specific potential E, and

ring collection efficiency (0.235), respectively.

$$\%H_2O_2 = 2 \times \frac{I_R/N}{I_D + I_R/N} \times 100 \quad (4)$$

3. Results and discussion

3.1. Electrochemical performance

Figure 1A compares the voltammetric curves of carbons containing N or N/S with that of a commercial electrocatalyst (EC20, 20% Pt). Pt has always the best performance in term of onset potential and limiting current. The presence of guanidine in the precursors shifts onset potential to more positive values, and a further improvement is observed when both of precursors, cysteine and guanidine, are used for the electrocatalyst preparation. In ZCG a better kinetic behaviour at high overpotentials (see Tafel slope and ΔE in Table 2) goes hand in hand with the appearance of a well-defined limiting current. This behaviour could be due both to the nature of nitrogen in the precursor that affects final electrocatalytic properties of the carbon, with aminic sp^3 nitrogen, as in cysteine, less favourable than sp^2 nitrogen bonded to sp^2 hybridized carbon, contained in guanidine, and/or to the presence of sulphur. The former could be justified considering different thermal stability of the two nitrogen and, therefore, different interactions with other elements during pyrolysis. The number of exchanged electrons is 4 for all samples, but the percentage of peroxide (Table 2, obtained from ring current reported in Fig S1A) is not negligible. Nevertheless, the smallest value, 17–18%, is obtained for ZG and ZCG. The co-presence of S, from cysteine, and N sp^2, from guanidine, seems beneficial to ORR but is not sufficient to equal the performance of reference electrocatalyst, EC20.

Interestingly, by doping with iron and/or copper, the picture completely changes (Fig. 1B, Fig. S1B Tab. 2). The doping with a single metal improves the performance of these materials. In particular, in the case of iron-doped samples, results are even better than for platinum, especially in the case of carbons prepared with a mixture of cysteine and guanidine (ZCG series, see Table 2 and Fig. 1B). Onset potential is more positive of about 30 mV (Pt 0.923 vs RHE/V, ZCGFe 0.953 vs RHE/V) and the maximum peroxide yield is about 7%. Nevertheless, number of exchanged electrons, ΔE, and Tafel slopes at low and high overpotentials do not show significant variations. As already observed for metal-free samples, the use of a nitrogen sp^2 derivative in the precursors shifts onset potentials to more positive values than those obtained in the case of nitrogen sp^3 containing compounds (Table 2). The co-doping with iron and copper does not enhance the performance compared to single doping with iron. In conclusion, considering all data in Table 2, a sort of electrocatalytical activity scale can be built: ZC < ZG < ZCG << ZCGCu << ZCFe < ZCFeCu < Pt (EC20) < ZGFeCu < ZGFe ≈ ZCGFeCu < ZCGFe.

In order to rationalize and comprehend these data a deep physico-chemical characterization is necessary.

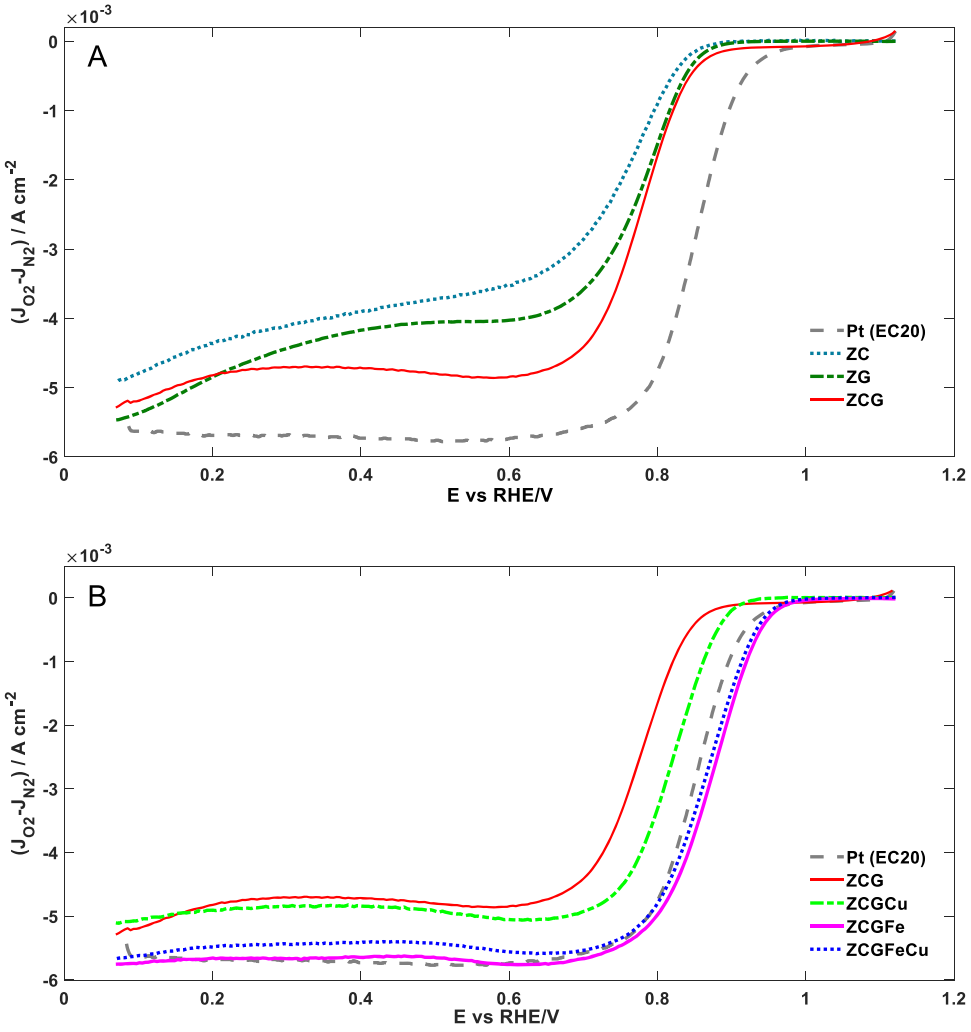

Fig. 1. Cyclic Voltammetry, T = 25 °C, 0.1 M KOH, ν = 5 mV s^{-1}, ω= 1600 rpm. A) on catalysts with different heteroatoms; B) on catalysts containing different metals.

Table 2
Electrochemical Data.

	E_{on}, Onset Potential* vs RHE/V	$E_{1/2}$* vs RHE/V	$\Delta E=(E_{on}-E_{1/2})$ / V	Tafel Slope $\left(\frac{\partial \eta}{\partial \ln J}\right)$ V		Maximum of H_2O_2%	n. e^-
				Low η	High η		
EC20 (20% Pt)	0.923	0.854	0.069	0.026	0.050	4	4.0
ZC	0.836	0.784	0.052	0.020	0.049	28	4.6 ± 0.2
ZG	0.849	0.796	0.053	0.019	0.038	17	4.45 ± 0.06
ZCG	0.852	0.780	0.072	0.028	0.042	18	4.2 ± 0.2
ZCFe	0.922	0.845	0.077	0.031	0.065	8	4.19±0.03
ZGFe	0.945	0.879	0.066	0.022	0.040	6	4.090±0.003
ZCGFe	0.953	0.879	0.074	0.024	0.056	7	4.116 ± 0.004
ZCGCu	0.888	0.827	0.061	0.019	0.052	13	4.255 ± 0.006
ZCFeCu	0.910	0.839	0.071	0.014	0.035	16	4.1 ± 0.1
ZGFeCu	0.942	0.875	0.067	0.017	0.104	4	4.09±0.03
ZCGFeCu	0.942	0.871	0.071	0.021	0.043	4	4.055 ± 0.002

* Standard deviation is about 2 mV for all data.

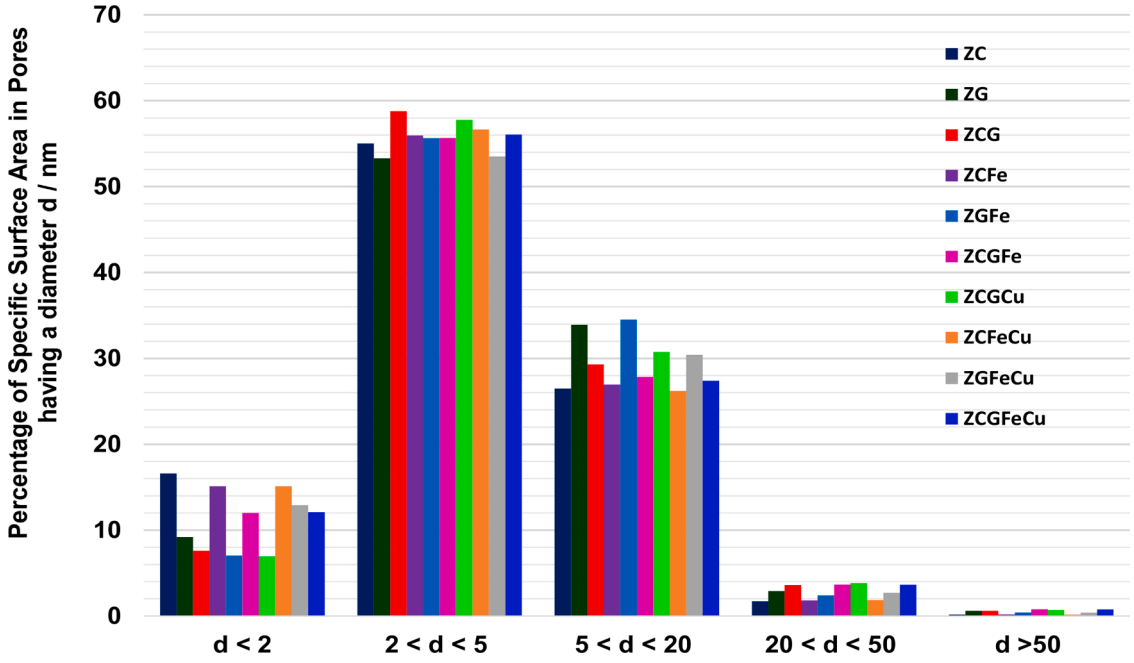

Fig. 2. Porosity Distribution: Percentage of Specific Surface Area in pores having a diameter d / nm.

3.2. *Specific surface area and pore size distribution*

Nitrogen adsorption-desorption isotherms of all samples, reported in Fig. S2, are classified of type IV with hysteresis loops according to IUPAC classification [44]. This isotherm is typical of mesoporous materials with a hierarchical pores structure, beneficial for ORR [45]. However, the loop behaviour depends in a complicated way on the considered material. In the case of materials prepared by using only cysteine (ZC family), the loop is a H5 type [44], associated with pore structures containing both open and partially blocked cylindrical mesopores [44]. The two knees in the desorption part indicate the occurrence of both equilibrium evaporation/desorption and cavitation effects. At higher pressure, desorption is related to the evaporation from open pores, while blocked mesopores remain filled until they empty by cavitation [46]. All remaining carbons are characterized by a more or less evident H3 type loop, typical of materials presenting either non-rigid aggregates of plate like particles, or macropores non completely filled by pore condensate [44].

Figure 2 displays the pore size distributions of the investigated electrocatalysts. The percentage of micropores, comprised between ~10 and 20%, confirms their mesoporous nature. The materials do not significantly differ from each other, being all characterized by small mesopores ($2<d<5$ nm), accompanied by larger mesopores, which constitute a well-organized lung-like structure, beneficial to diffusion/retro-diffusion of reactants and products. This behaviour may be due to the specific templating method adopted during the synthesis.

For most samples, specific surface area (Table 3) is comprised

Table 3
Specific surface area, pore volume, and micropore volume of the samples.

Sample Name	Specific Surface Area $m^2\ g^{-1}$	Total Pore Volume $cm^3\ g^{-1}$	Meso- + Macro-Pore Volume $cm^3\ g^{-1}$	Micropore Volume $cm^3\ g^{-1}$
ZC	414	0.56	0.53	0.03
ZG	662	1.28	1.25	0.03
ZCG	628	1.17	1.15	0.02
ZCFe	375	0.51	0.49	0.02
ZGFe	702	1.28	1.26	0.02
ZCGFe	759	1.48	1.44	0.04
ZCGCu	656	1.27	1.25	0.02
ZCFeCu	355	0.48	0.46	0.02
ZGFeCu	653	1.19	1.15	0.04
ZCGFeCu	759	1.47	1.43	0.04

between 560 and 760 $m^2\ g^{-1}$, a typical range obtained by templating with the specific SiO_2 powder used in this work [30,31]. However, all samples of ZC family have both specific surface area (about 40–45%) and meso – macro- pore volume (Table 3) lower than the corresponding samples of ZG family, while micropore volume is similar to that of the other samples. This behaviour could be justified considering that L-cysteine and guanidine acetate have different affinity toward silica. The melting point of both these N-containing compounds is about 230–240 °C (L-cysteine, T = 240 °C, and guanidine acetate, T = 226–230 °C). Above this temperature, while guanidinium, positively charged, easily adsorbs on partially hydroxylated negatively charged silica surface, L-cysteine, belonging to polar/neutral class of amino acids, interacts very little with its surface [47]. Consequently, while guanidinium species envelop silica, intimately assuming its nanometric shape and maintaining it during carbonization, L-cysteine flows away from silica hydroxylated surface, nullifying its templating properties.

3.3. Surface species

Table 4 reports the surface composition, as inferred from XPS results for all considered samples. The results are in line with the expectations.

The curve fitting of N1s XP spectra (Fig. S3 and Table 5), although the difficulty to properly attribute the fitted peaks [48], due to the superimposition of regions of each "nitrogen" [48] reveals the presence of many different types of nitrogen species on the surface of carbon samples, amongst them, pyridinic, hydrogenated (in-plane), protonated, hydrogenated- edge and Me-N_x nitrogen that are the most important for ORR electroactivity [48–50]. Indeed, the most electro-active materials (ZGFe, ZGFeCu, ZCGFe, and ZCGFeCu) show the highest amount of Me-N_x groups coupled with pyridinic N, beneficial to ORR [49]. Instead, the very largest amount of hydrogenated (in-plane) nitrogen, which preferentially forms peroxides compounds [48,49], is on the surface of ZC, ZG, ZCG and on ZCFeCu, the carbons that, as observed above and in accordance with electrochemical results, produce the largest amount of peroxide amongst all the samples studied in this work (Table 2). A similar quantity of hydrogenated nitrogen is also found in ZCGFeCu, though, in this case, the amount of produced H_2O_2 is low (Table 2). This apparent contradiction can be explained considering that the high quantity of pyridinic nitrogen in this sample favours the reduction of hydrogen peroxide to water [49].

Fig. S4 and Table 6 display the results of S2p XP spectra curve fitting of samples prepared by using cysteine. On the surface, there are different sulphur functional groups: S bonded to metal (B.E. 162–162.3 eV), thiophene-like S or S-H (B.E. 164.0 – 164.2 eV), $S = O$ (B.E. 166.0 – 167.0 eV), and finally S(O)O (B.E. 168.5 – 169.5 eV) [29,51–54]. Sulphur bonded to metal is peculiarly found only in the samples of ZC series and not in ZCG family. An explanation of this behaviour excludes a preferential formation of Me-S sites instead of Me-N_x in ZC series since Me-N_x-percentage is quite similar for all the considered samples (ZC and ZCG families, Table 6), so another justification is necessary, and a possible preferential formation of metal compounds in ZC carbons, as sulphides or sulphates, should be invoked. Unfortunately, due to the low ratio signal/noise, Fe *2p* spectra are not useful to validate this hypothesis. The highest amount of thiophene-like functionalities, beneficial to ORR [52,55,56], is found in metal-doped ZCG samples. It seems that the presence of N sp^2 in the precursor of carbons favours the formation of this functional group and so the formation of very active materials to the detriment of the formation of oxidized sulphur, not useful for ORR [51], but abundant in the other less active samples.

From the XPS data, it is evident that the best catalysts, ZCGFe and ZCGFeCu, contain a high amount of pyridinic nitrogen coupled with Me-N_x and the highest quantity of SH/thiophene-like S. It is possible to hypothesize an interaction between N-functionalities and S-H/thiophene-like groups with the building of a local collaborative structure [57], like a very active S-doped metal-N_x-C site. This hypothesis might be supported by some literature results showing that the breaking of O—O is easier in a similar catalytic site than in a not-S-containing equivalent [28].

3.4. Electrocatalyst structure

Figure 3A compares the low 2θ portions of the XRPD patterns of metal-free catalysts and crystalline graphite. Rietveld refinements reveal that catalysts are single phase, with graphite space group $P6_3mc$ (see Figs. S5A and S5B and Tab. S1). The broadening of the peaks points to the reduction of crystalline coherence with respect to graphite.

The shift of the maximum of the most intense reflection (002) toward lower 2θ values suggests an expansion of the c axis. According to the Rietveld analysis, c passes from ≈6.735 Å in graphite (in agreement with the literature [58]) to 7.23–7.29 Å (see Tab. S1). In addition (002) reflections of carbon samples are asymmetric, probably as a consequence of strain effects.

Figure 3B shows the low 2θ portions of the XRPD patterns of Fe doped catalysts. Additional sharper peaks are here visible. The phase analysis reveals peaks of FeS throlite phase [59] in the patterns of ZCFe and in ZCGFe. Their relative intensity suggests a dependence of FeS amount on the concentration of cysteine in the precursors. Body- and/or face-centred cubic (bcc [60] and fcc, austenite [61]) Fe structures, are detected in all catalysts except in ZCFe (see Tab. S1B).

The increasing asymmetry of the graphite (002) peak with the guanidine concentration in the precursors (see ZCFe, ZCGFe and ZGFe samples) points to an active role of metals during the synthesis of the C phase.

Cu_2S [62] and fcc metal Cu [63] are detected in the XRPD patterns of ZCGCu and ZCGFeCu samples (Fig. 3C). In ZCGFeCu sample, also the peaks FeO wustite phase are present. Fe and FeS phases are absent in both Cu and Fe-Cu double doped samples. Rietveld refinements confirmed the phase analysis (see Tab. S1C and Fig.S5C).

Figure 3D shows the full G(r) functions of metal free catalysts, while their low r regions are displayed in Fig. S6. The RSRA reveals that their coherence length is shorter than in graphite (≈ 15 Å against ≈ 80 Å, see Fig. 3D, Fig. S7, and Tab. S2). Moreover, the nearest neighbour (NN) C—C distance is slightly greater (≈ 1.420(4) Å against ≈ 1.414(4) Å in graphite). This small expansion may be related to scarce coherence also along the ab plane, with graphite-like clusters formed by few hexagons featured by bonds with an increased sp^3 character at their borders. Moreover, the peak broadening points to an increased disorder and to a reduced crystallographic coherence with respect to graphite, especially along the c direction.

Figure 3E compares the G(r) functions of metal free and selected

Table 4
Surface elemental composition of the catalysts.

	ZC	ZG	ZCG	ZCFe	ZGFe	ZCGFe	ZCFeCu	ZGFeCu	ZCGFeCu
%C	~91	~92	~90	~90	~90	~90	~90	~89	~90
%N	~4	~6	~6	~4	~5	~5	~4	~5	~5
%O	~4	~3	~3	~4	~5	~4	~5	~5	~4
%S	0.8	–	0.4	~1	–	0.5	~1	–	0.6
%Fe	–	–	–	0.3	0.4	0.3	0.2	0.3	0.3
%Cu	–	–	–	–	–	–	0.1	0.2	0.1

Table 5
Results of the curve fitting of the high-resolution N1s XP spectra.

Peak	BE / eV	Functional group	ZC	ZG	ZCG	ZCFe	ZGFe	ZCGFe	ZCFeCu	ZGFeCu	ZCGFeCu
1)	398.3 – 398.5	Pyridinic N	17	16	16	16	19	19	15	19	20
2)	399.2 – 399.6	N_x–Me or amine	10	10	6	10	11	6	8	11	7
3)	400.9 – 401.0	Hydrogenated (in-plane)/	43	40	45	42	40	38	46	41	46
4)	402.0 – 403.0	Protonated	13	13	14	13	13	19	14	12	13
5)	403.3 – 403.6	Hydrogenated Edge	7	7	9	7	7	6	7	7	6
6)	404.8 – 405.1	Oxidized N	6	8	7	7	6	6	7	6	4
7)	406.8 – 406.9	Shake up π – π*	4	6	3	4	4	5	4	4	5

Table 6
Results of the curve fitting of the high-resolution S2p XP spectra.

Peak	BE / eV	Functional group	ZC	ZCFe	ZCFeCu	ZCG	ZCGFe	ZCGFeCu
1)	162.0 – 162.3	S-Me	–	4	3	–	–	–
2)	164.0 – 164.2	SH or thiophene-like S	74	74	75	68	86	89
3)	166.0 – 167.0	$S=O$	16	15	11	20	–	–
4)	168.5 – 169.5	S(O)O	10	7	11	12	14	11

metal doped ZCG samples. The differences at large r values suggest that the crystal coherence of metal phases is larger than the carbon one. Small lengthening of this C—C distance appears in all doped samples with respect to the undoped ones (Tab.S3). This finding points to a metal-induced change in the sp^2-sp^3 ratio in the carbon phase.

As ZCGFe contains too many phases, RSRA was limited to ZCFe and ZGFe. The results are displayed in Tab. S4, while some examples of fits are reported in Fig. S8. The formation of FeS phase in ZCFe and ZCGFe, and of bbc-Fe in ZGFe is confirmed. The weight fraction of FeS phase computed by RSRA is larger than obtained from the Rietveld refinements for both ZCFe [0.07(1) *vs* 0.0194(4)] and ZCGFe [0.05(1) *vs*. 0.0014(3)] samples. This suggests that, beside the crystals detected by the Rietveld analysis, also FeS like structures with very short structural coherence exist in the samples prepared with cysteine. Additional analysis of the G(r) functions, as well as some examples of fits of doped samples, are reported in the SI section (Fig.S8).

Figure 4A displays the micro-Raman spectra of some of the investigated catalysts. The D- and G-bands, typical of highly disordered graphitic nanocarbons, dominate the spectra of all the samples, confirming their amorphous nature. The former band (at ~1346 cm^{-1}, for 2.33 eV excitation) originates from the A_{1g} symmetry in-plane breathing-mode of the C hexagonal rings and is disorder-activated. The latter, commonly regarded as the Raman fingerprint of the graphitic crystalline arrangement, is associated to the E_{2g} symmetry stretching of all sp^2 bonded C = C pairs [64]. At higher frequency (>2000 cm^{-1}), a weaker and broader featureless second-order structure is further detected. As known [64], clustering of the sp^2 phase, presence of sp^2 rings or chains, local distortions, and hybridisation changes of the C–C bonding act as competing forces on the shape of the Raman spectra of nanocarbons. In order to monitor the changes produced by the addition of guanidine-, iron- and/or copper-acetate in the precursor sugar/cysteine mixture, according to the most recent trends on the analysis of Raman spectra of amorphous nanocarbons [65], the 800−1900 cm^{-1} region of the spectra was fitted to Gaussian-Lorentzian lineshapes (Fig. S9). Four bands were necessary to reproduce the spectra, namely, the D- and G-bands and, besides, two weaker features, indicative of the presence of trans-poly-acetylene-like chains (T-band at 1130−1230 cm^{-1}), formed at the zig-zag edges of the defective graphitic layers, and of amorphous phases (A-band at 1450−1530 cm^{-1}), connected to the planes of the aromatic rings through Csp^3 bonds [66–68]. Frequency positions (ω) and widths (γ, FWHM) of these bands are reported in Tab. S5, together with the average size of the graphitic domains (L_C), as calculated from the D/G integrated intensity ratio (I_D/I_G), via the relationship proposed by Tuinstra-Koenig [69] L_C, ranging between 1.3 and 1.9 nm, decreases in the order ZC > ZCG > ZCGCu > ZCGFe > ZCGFeCu, indicating that larger domains with graphitic order are formed in the carbonaceous matrix in the absence of guanidine-acetate for metal-free catalysts, and of iron- and/or copper-acetate for Fe- and/or Cu-containing catalysts.

The frequency position of the G-band (ω_G) that gives a measure of the strength of C bonding and is sensitive to charge transfer, tensile strain/compressive stress and hybridisation changes of the C–C bonding [67] increases in the order ZC (1587.0 cm^{-1}) < ZCG (1589.7 cm^{-1}) < ZCGCu (1591.0 cm^{-1}) < ZCGFeCu (1594.8 cm^{-1}) < ZCGFe (1595.1 cm^{-1}). The upshift is accompanied by the progressive shrinking of the band (see γ_G in Tab. S5). Based on the current assessments on the interpretation of Raman spectra of nanocarbons [67,68,70], these changes hints at the presence of short chains of strained C = C bonds, deriving from polymerized organics [70]. The presence of strain effects on the carbon phase induced by metals was also suggested by the asymmetry of the (002) peaks in XRPD experiments (see Fig. 3).

Recently, it has been reported that molecular oxygen preferentially interacts with defects having partial radical character located at the zigzag-shaped edges of graphene/graphite [67,71,72]. These localised electronic states act as paramagnetic centres [73]. As Csp^3 and Csp^2 defects contribute to the intensities of the A- and D-bands, respectively [64,66], their relative density was estimated as integrated intensity ratio of the two bands (I_A/I_D). The ratio is found to increase in the order ZC < ZCG < ZCGCu < ZCGFeCu < ZCGFe, *i.e.* in the same order as ω_G. A good correlation with the electrochemical results is observed (Fig. 4B): the lowest and highest densities of localised Csp^3 defects (with respect to the sp^2 ones) pertain to catalysts ZC and ZCGFe, exhibiting the worst and the best performance towards the ORR, respectively. This fully agrees with the enhanced activity caused by the increase of sp^3-hybridized carbon defects reported by Cao et al. [74]. Besides to the presence of specific defects in the graphite-like C network (C atoms and C–C bonds with specific charge density due to the presence of nearlying heteroatoms, defects or vacancies, all behaving as active sites [75]), the increase of sp^3 hybridization might be associated to the increase in curvature of the graphene-like planes, *i.e.* to the formation of nanostructures such as nanotubes [76,77].

Indeed, a good correlation seems to exist also between the average size of the graphitic domains and the limiting current (Fig. 4C): the smaller L_C, the higher the limiting current. This is not surprising as L_C gives a measure of the inter-defect in-plane distance in the graphite-like network, and it reduces with increasing both intrinsic defects, such as armchair and zigzag edge defects, point defects (*e.g.*, vacancies, holes, and voids), line defects (*e.g.*, dislocation, grain boundaries), topological defects (*e.g.*, pentagon, heptagon, Stone–Wales defects), and extrinsic defects (*e.g.*, heteroatoms and/or metal dopants), which all contribute to increase the active surface area and the electrocatalyst reactivity [78]. Although MRS can only roughly characterize the density and the types of defects, the ORR activity is the determination of the edge and defect

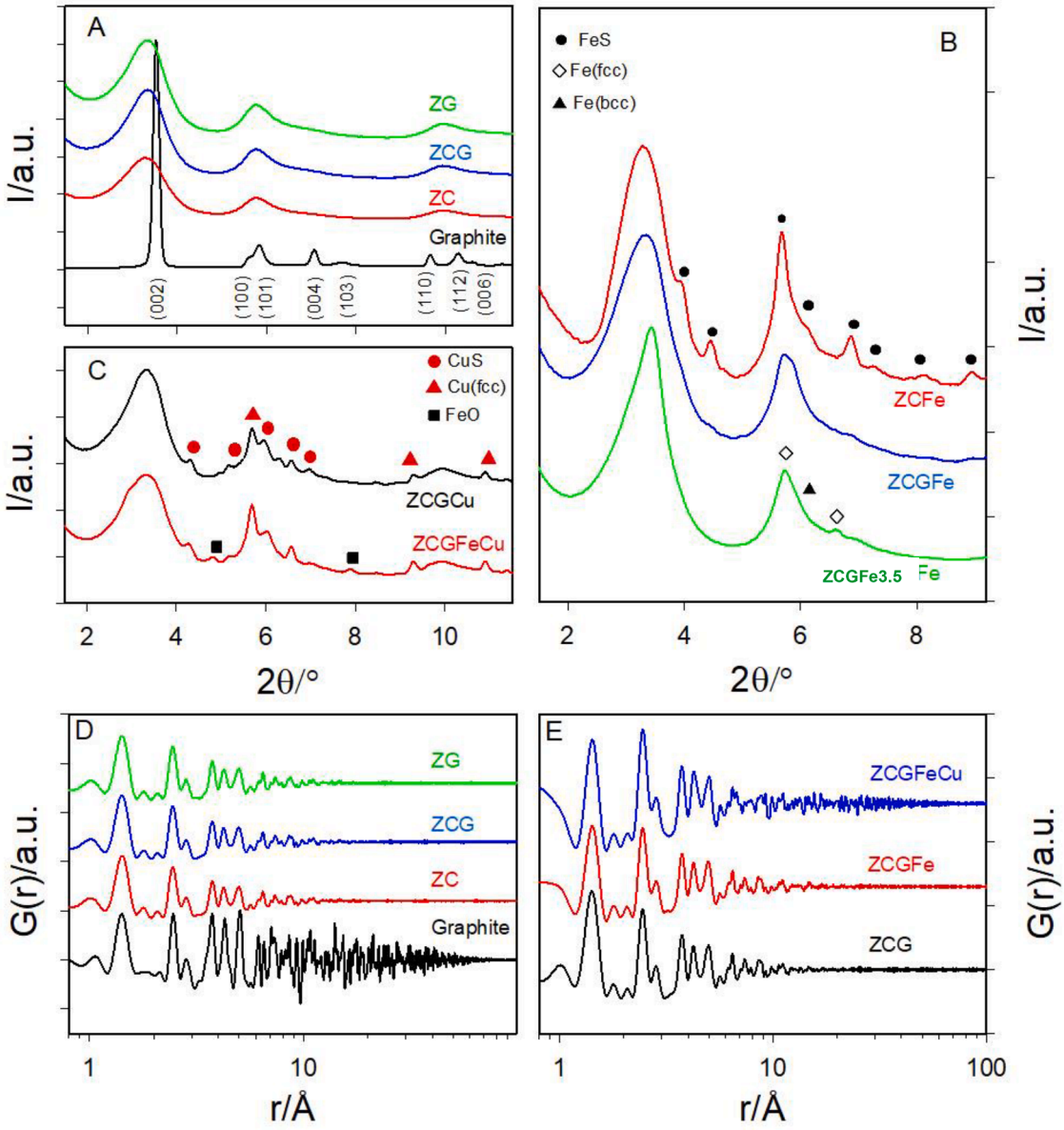

Fig. 3. A) Details of the XRPD patterns pertinent to pure carbon samples. Numbers into brackets are the Miller indexes of graphite Bragg peaks. B) Details of the XRPD patterns pertinent to Fe single doped carbon samples. C) Details of the XRPD patterns pertinent to Cu-containing carbon samples. In Panels B and C, symbols are placed in correspondence of reflections of metal containing phases. D) G(r) functions of metal-free samples. E) Selected G(r) functions of metal free and metal doped ZCG samples.

density, as recently claimed by Zhang et al. [78].

3.5. Morphology

Figure 5 and Fig. S10 show SEM images of the catalysts. In the series of materials prepared without metals, ZC, ZG and ZCG, the dominant structure is a sponge-like type, as expected from the used synthesis path [31,79] and no other structure can be seen.

Conversely, all the samples doped with iron (ZCFeCu, ZGFeCu, ZCGFe, ZCGFeCu) show filamentous nanostructures, with different length and structures depending on sample, grafted onto the massive part of the carbon, and it must be noted that these characteristic structures are completely absent in the other materials, not only in metal-free materials but also in the carbon containing only copper. This is in accordance both with diffraction results, which, as discussed above, show that the addition of iron modifies the carbon phase structure, and with the indications emerging from Raman analysis, signalling spectral changes which might arise also from the increased curvature of the graphene-like planes.

For materials containing sulphur and metals (ZCFe, ZCFeCu) in addition to the sponge-like structure, a rock-like one is observed and, in the case of ZCFe, some ribbon-like carbon structures can also be seen. Moreover, the filamentous nanostructures mentioned above can be observed only in the presence of globular or polyhedral structures, based on metal sulfides (see EDX in Tab. S6), and, in particular for ZCFeCu very nice octahedral structures are detected based on a copper rich sulfide doped with iron (Cu:Fe:S = 5:1:3), confirming XPS results. Furthermore, nano filaments in ZCFe show some bulges in many positions, at the bottom, at the top, or in some cases in the middle. These bulges are based on sulfides derivatives (Tab. S6).

ZGFe, containing nitrogen and iron, is characterized by a dominant sponge-like structure with some rock-like pieces. Wires are widespread and very long.

Adding copper (ZGFeCu) modifies the morphology. In fact, although

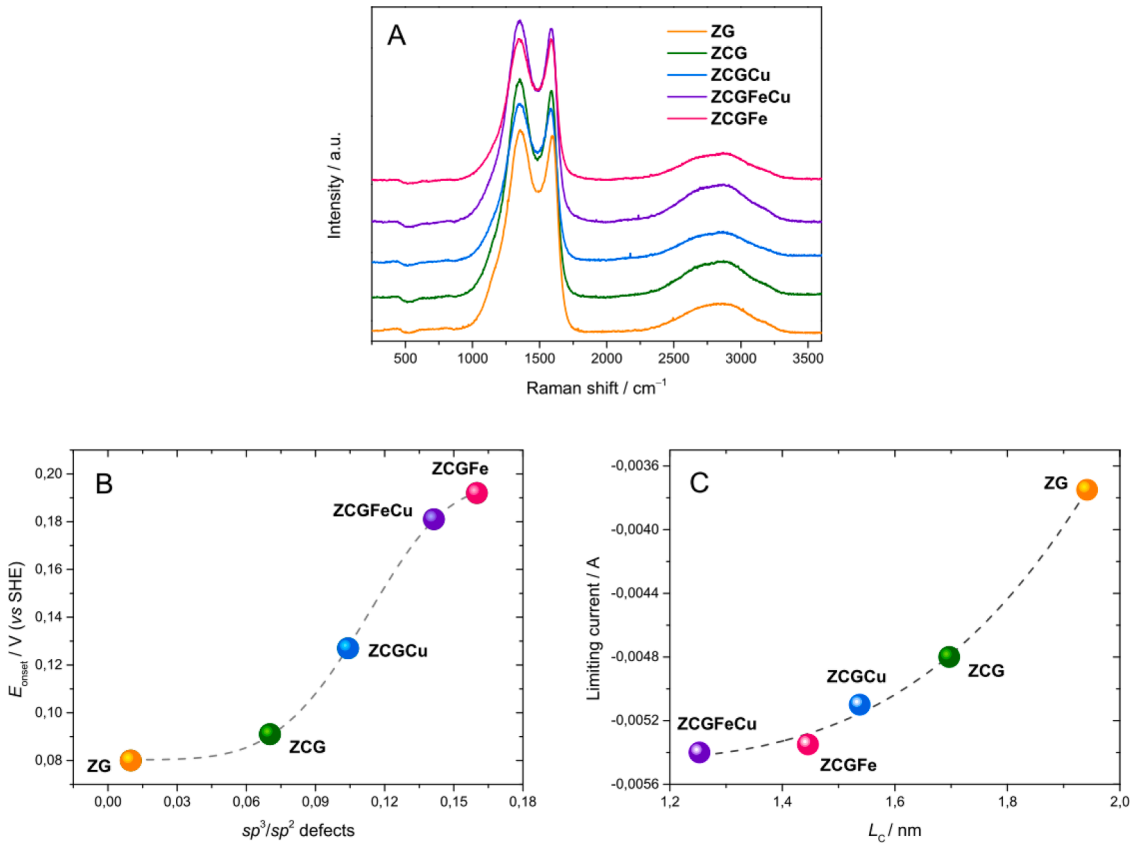

Fig. 4. A) Micro-Raman spectra of the catalysts; B) and C) Correlations between electrochemical results and descriptive parameters inferred from the analysis of the spectra: B) onset potential (E_{onset}) as a function of Csp^3 to Csp^2 defect density; C) limiting current as a function of the inter-defect in-plane distance (L_C) in the graphite-like network.

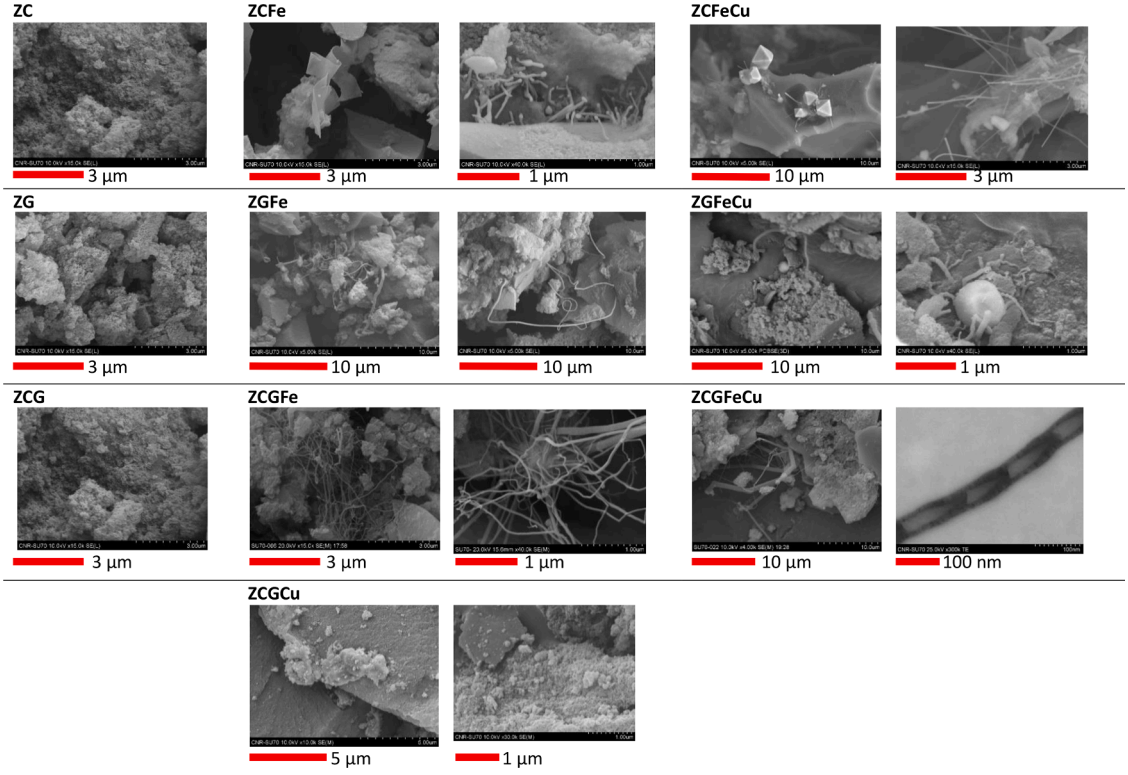

Fig. 5. Scanning electron microscopy images. Marker size is reported below each image (Red bar).

the general structure looks like that of ZGFe, nanowires are not so widespread as in ZGFe, and some globular twisted tubes can be seen and some copper particles (see Tab. S6) well crystallized and faceted are set down on sponge-like structure.

These results show that it is possible to obtain co-doped materials with nitrogen and sulphur with carbon filamentous structures grafted onto their surface through a facile synthesis path. Results further confirm that iron, unlike copper, is a material forming carbonaceous structures in specific conditions [80–82]. Carbonaceous filaments have a bamboo-like architecture, with walls built by superimposition of other nanostructures (ZCGFeCu), they are more widespread in ZCGFe than in ZCGFeCu, where also copper particles are visible. In these materials, sulfides are not detected, since probably nitrogen hinders their formation, subtracting metals. No filaments are observed in ZCGCu, featured by a sponge-like structure.

It is remarkable that the most active materials, ZCGFe and ZCGFeCu, characterized by a high amount of pyridinic nitrogen coupled with Fe-Nx and the highest quantity of SH/thiophene-like S, as previously observed in Par. 3.3, are those with nanotubes grafted onto the surface. Moreover, ZCGFe, the most active of the whole series, is the sample with the most widespread nanotubes, evidencing the existence of a correlation between the presence of these nanostructures and the electrocatalytic activity.

4. Conclusions

An easy procedure has been presented to synthesise ORR electrocatalysts, consisting in sulphur- and/or nitrogen-modified carbons, some of which iron- and/or copper-doped. Bamboo-like filamentous nanostructures, grafted onto the surface of iron-containing electrocatalysts, play a crucial role in enhancing the electrochemical performance. Their length and morphology depend on the precursors utilized in the synthesis. The most active materials toward ORR contain pyridine-like and Fe-N_x nitrogen species coupled with thiophene-like sulphur. This picture points to the occurrence of synergistic effects between heteroatoms and active sites associated to the presence of nanotubes.

CRediT authorship contribution statement

Erlind Mysliu: Methodology, Formal analysis, Investigation, Writing – original draft. **Marco Scavini:** Methodology, Formal analysis, Investigation, Resources, Data curation, Writing – original draft, Visualization, Funding acquisition. **Saveria Santangelo:** Methodology, Formal analysis, Investigation, Resources, Data curation, Writing – original draft, Writing – review & editing, Visualization. **Salvatore Patanè:** Methodology, Formal analysis, Investigation, Resources, Data curation, Writing – original draft. **Nicoletta Ditaranto:** Methodology, Formal analysis, Investigation, Resources, Data curation, Writing – original draft, Visualization. **Paola Bassani:** Methodology, Formal analysis, Investigation, Resources, Data curation. **Mariangela Longhi:** Conceptualization, Methodology, Formal analysis, Investigation, Resources, Data curation, Writing – original draft, Writing – review & editing, Visualization, Supervision, Funding acquisition.

Declaration of Competing Interest

The authors declare that they have no known competing financial interests or personal relationships that could have appeared to influence the work reported in this paper.

Data availability

Data will be made available on request.

Acknowledgments

Funding: This work was supported by the Università degli Studi di Milano (“Pt-free catalysts for oxygen reduction reaction in PEMFCs“, Piano di Sostegno alla ricerca, Linea 2). M.L and M.S. acknowledge partial funding under the National Recovery and Resilience Plan (NRRP), Mission 4 Component 2 Investment 1.3 - Call for tender No. 1561 of 11.10.2022 of Ministero dell’Università e della Ricerca (MUR); funded by the European Union – NextGenerationEU (Project code PE0000021, Concession Decree No. 1561 of 11.10.2022 adopted by Ministero dell’Università e della Ricerca (MUR), CUP D43C22003090001, Project title “Network 4 Energy Sustainable Transition – NEST”). Authors acknowledge DESY (Hamburg, Germany), a member of the Helmholtz Association HGF, for the provision of experimental facilities and Dr. Martin Etter for collecting XRPD data. Parts of this research were carried out at PETRA III, beamline P02.1 within the rapid access program 2021A under proposal ID RAt-20010264. Dr. Mauro Coduri is also acknowledged by one of the authors (MS) for useful discussions.

Supplementary materials

Supplementary material associated with this article can be found, in the online version, at doi:10.1016/j.electacta.2023.142946.

References

[1] Sustainable Development Goals, United Nations, https://www.un.org/sustainabledevelopment/, (accessed 05/08/2022), (n.d.). 10.1021/cr020730k.
[2] Y. Yuan, J. Lu, Demanding energy from carbon, Carbon Energy 1 (2019) 8–12, https://doi.org/10.1002/cey2.12.
[3] C. Hu, Q. Dai, L. Dai, Multifunctional carbon-based metal-free catalysts for advanced energy conversion and storage, Cell Rep. Phys. Sci. 2 (2021), 100328, https://doi.org/10.1016/J.XCRP.2021.100328.
[4] M. Winter, R.J. Brodd, What Are Batteries, Fuel Cells, and Supercapacitors? Chem. Rev. 104 (2004) 4245–4269, https://doi.org/10.1021/cr020730k.
[5] D. Yan, Y. Li, J. Huo, R. Chen, L. Dai, S. Wang, Defect chemistry of nonprecious-metal electrocatalysts for oxygen reactions, Adv. Mater. 29 (2017), 1606459, https://doi.org/10.1002/adma.201606459.
[6] M. Nestoridi, D. Pletcher, R.J.K. Wood, S. Wang, R.L. Jones, K.R. Stokes, I. Wilcock, The study of aluminium anodes for high power density Al/air batteries with brine electrolytes, J. Power Sources 178 (2008) 445–455, https://doi.org/10.1016/J.JPOWSOUR.2007.11.108.
[7] S. Zhang, X.Z. Yuan, J.N.C. Hin, H. Wang, K.A. Friedrich, M. Schulze, A review of platinum-based catalyst layer degradation in proton exchange membrane fuel cells, J. Power Sources 194 (2009) 588–600, https://doi.org/10.1016/J.JPOWSOUR.2009.06.073.
[8] R. Jasinsky, A new fuel cell cathode catalyst, Nature 201 (1964) 1212–1213, https://doi.org/10.1038/2011212a0.
[9] F. Jaouen, J. Herranz, M. Lefè, J.-P. Dodelet, U.I. Kramm, I. Herrmann, P. Bogdanoff, J. Maruyama, T. Nagaoka, A. Garsuch, J.R. Dahn, T. Olson, S. Pylypenko, P. Atanassov, E.A. Ustinov, Cross-laboratory experimental study of non-noble-metal electrocatalysts for the oxygen reduction reaction, ACS Appl. Mater. Interfaces 1 (2009) 1623–1639, https://doi.org/10.1021/am900219g.
[10] Y. Chen, Y. Huang, M. Xu, T. Asset, X. Yan, K. Artyushkova, M. Kodali, E. Murphy, A. Ly, X. Pan, I.v. Zenyuk, P. Atanassov, Catalysts by pyrolysis: direct observation of transformations during re-pyrolysis of transition metal-nitrogen-carbon materials leading to state-of-the-art platinum group metal-free electrocatalyst, Mater. Today 53 (2022) 58–70, https://doi.org/10.1016/J.MATTOD.2022.01.016.
[11] U. Martinez, S. Komini Babu, E.F. Holby, H.T. Chung, X. Yin, P. Zelenay, Progress in the development of Fe-Based PGM-free electrocatalysts for the oxygen reduction reaction, Adv. Mater. 31 (2019), 1806545, https://doi.org/10.1002/adma.201806545.
[12] K. Guo, N. Li, L. Bao, P. Zhang, X. Lu, Intrinsic carbon structural imperfections for enhancing energy conversion electrocatalysts, Chem. Eng. J. 466 (2023), 143060, https://doi.org/10.1016/j.cej.2023.143060.
[13] M. Zhang, L. Dai, Carbon nanomaterials as metal-free catalysts in next generation fuel cells, Nano Energy 1 (2012) 514–517, https://doi.org/10.1016/J.NANOEN.2012.02.008.
[14] H. Zeng, W. Wang, J. Li, J. Luo, S. Chen, In Situ generated dual-template method for Fe/N/S Co-Doped hierarchically porous honeycomb carbon for high-performance oxygen reduction, ACS Appl. Mater. Interfaces 10 (2018) 8721–8729, https://doi.org/10.1021/acsami.7b19645.
[15] Y. Jia, X. Yao, Defects in carbon-based materials for electrocatalysis: synthesis, recognition, and advances, Acc. Chem. Res. 56 (2023) 948–958, https://doi.org/10.1021/acs.accounts.2c00809.

[16] S. Kattel, G. Wang, A density functional theory study of oxygen reduction reaction on Me-N 4 (Me ¼ Fe, Co, or Ni) clusters between graphitic pores, J. Mater. Chem. A Mater. 1 (2013) 10790–10797, https://doi.org/10.1039/c3ta12142a.

[17] M.J. Dzara, K. Artyushkova, T. Sougrati, C. Ngo, M.A. Fitzgerald, A. Serov, B. Zulevi, P. Atanassov, F. Frédé, F. Jaouen, S. Pylypenko, Characterizing complex gas−solid interfaces with in Situ spectroscopy: oxygen adsorption behavior on Fe−N−C catalysts, J. Physi. Chem. C 124 (2020) 16529–16543, https://doi.org/10.1021/acs.jpcc.0c05244.

[18] J. Li, M. Tahar Sougrati, A. Zitolo, J.M. Ablett, I. Can Oğuz, T. Mineva, I. Matanovic, P. Atanassov, Y. Huang, I. Zenyuk, A. Cicco, K. Kumar, L. Dubau, F. Maillard, G. Dražić, F. Jaouen, Identification of durable and non-durable FeNx sites in Fe–N–C materials for proton exchange membrane fuel cells, Nat Catal 4 (2021) 10–19, https://doi.org/10.1038/s41929-020-00545-2.

[19] L. Chen, Z.-H. Huang, H.-W. Liang, H. Gao, S.-H. Yu, Three-dimensional heteroatom-doped carbon nanofiber networks derived from bacterial cellulose for supercapacitors, Adv. Funct. Mater. 24 (2014) 5104–5111, https://doi.org/10.1002/adfm.201400590.

[20] X. Wang, C. Yang, J. Li, an Chen, K. Yang, X. Yu, D. Lin, Q. Zhang, S. Wang, J. Wang, Z. Xia, H. Jin, X. Wang, Z. Xia, C. Yang, J. Li, X. Chen, K. Yang, X. Yu, D. Lin, Q. Zhang, S. Wang, H. Jin, J. Wang, Insights of heteroatoms doping-enhanced bifunctionalities on carbon based energy storage and conversion, Adv. Funct. Mater. 31 (2021), https://doi.org/10.1002/adfm.202009109, 2009109.

[21] H.Y. Wang, J.T. Ren, C.C. Weng, X.W. Lv, Z.Y. Yuan, Hierarchical porous N,S-codoped carbon with trapped Mn species for efficient pH-universal electrochemical oxygen reduction in Zn-air battery, J. Ind. Eng. Chem. 100 (2021) 92–98, https://doi.org/10.1016/J.JIEC.2021.05.037.

[22] J.C. Slater, Atomic radii in crystals, J. Chem. Phys. 41 (1964) 3199–3204, https://doi.org/10.1063/1.1725697.

[23] G. Periyasamy, K. Annamalai, I.M. Patil, B. Kakade, Sulfur and nitrogen co-doped rGO sheets as efficient electrocatalyst for oxygen reduction reaction in alkaline medium, Diam Rel. Mater. 114 (2021), 108338, https://doi.org/10.1016/J.DIAMOND.2021.108338.

[24] R. Verma, I. Chakraborty, S. Chowdhury, M.M. Ghangrekar, R. Balasubramanian, Nitrogen and sulfur codoped graphene macroassemblies as high-performance Electrocatalysts for the oxygen reduction reaction in microbial fuel cells, ACS Sustain. Chem. Eng. 8 (2020) 16591–16599, https://doi.org/10.1021/acssuschemeng.0c05909.

[25] J.P. Paraknowitsch, A. Thomas, Doping carbons beyond nitrogen: an overview of advanced heteroatom doped carbons with boron, sulphur and phosphorus for energy applications, Energy Environ. Sci. 6 (2013) 2839–2855, https://doi.org/10.1039/c3ee41444b.

[26] C. Yang, H. Jin, C. Cui, J. Li, J. Wang, K. Amine, J. Lu, S. Wang, Nitrogen and sulfur co-doped porous carbon sheets for energy storage and pH-universal oxygen reduction reaction, Nano Energy 54 (2018) 192–199, https://doi.org/10.1016/J.NANOEN.2018.10.005.

[27] G. Wu, Y. Nie, S Codoped N, Iron-carbon-based Electrocatalyst for Oxygen Reduction Reaction via Salt Recrystallization Strategy, Chem. Lett. 50 (2021) 124–127, https://doi.org/10.1246/cl.200643.

[28] X. Yan, X. Li, C. Fu, C. Lin, H. Hu, S. Shen, G. Wei, J. Zhang, Large specific surface area S-doped Fe–N–C electrocatalysts derived from Metal–Organic frameworks for oxygen reduction reaction, Progr. Natural Sci. 30 (2020) 896–904, https://doi.org/10.1016/J.PNSC.2020.10.018.

[29] B. Wu, J.-L. Mi, H. Hu, Z.-Y. Zu, L. Liu, Fe-, S-, and N-doped carbon nanotube networks as electrocatalysts for the oxygen reduction reaction, ACS Appl. Nano Mater 3 (2020) 12297–12307, https://doi.org/10.1021/acsanm.0c02789.

[30] M. Longhi, C. Cova, E. Pargoletti, M. Coduri, S. Santangelo, S. Patanè, N. Ditaranto, N. Cioffi, A. Facibeni, M. Scavini, Synergistic effects of active sites' nature and hydrophilicity on the oxygen reduction reaction activity of Pt-free catalysts, Nanomaterials 8 (2018) 643, https://doi.org/10.3390/nano8090643.

[31] M. Longhi, S. Marzorati, S. Checchia, B. Sacchi, N. Santo, C. Zaffino, M. Scavini, Sugar-based catalysts for oxygen reduction reaction. Effects of the functionalization of the nitrogen precursors on the electrocatalytic activity, Electrochim. Acta 222 (2016) 781–792, https://doi.org/10.1016/j.electacta.2016.11.036.

[32] S. Lowell, J.E. Shields, Powder Surface Area and Porosity, Third, Chapman & Hall Ltd, London, 1991.

[33] A.P. Hammersley, FIT2D V9.129 reference manual V3.1, ESRF98HA01T, 1998.

[34] H. Putz, Match! Phase Identification from Powder Diffraction, (2016).

[35] A.C. Larson, R.B. von Dreele, General Structural Analysis System (GSAS), LAUR, Los Alamos, 2004, pp. 86–748.

[36] T. Egami, S.J.L. Billinge, Underneath Bragg peaks, Pergamon Mater. Ser. (2003).

[37] P. Juhás, T. Davis, C.L. Farrow, S.J.L. Billinge, PDFgetX3: a rapid and highly automatable program for processing powder diffraction data into total scattering pair distribution functions, J. Appl. Crystallogr. 46 (2013) 560–566, https://doi.org/10.1107/S0021889813005190.

[38] M. Coduri, M. Brunelli, M. Scavini, M. Allieta, P. Masala, L. Capogna, H.E. Fischer, C. Ferrero, Rare Earth doped ceria: a combined X-ray and neutron pair distribution function study, Zeitschrift Für Kristallographie 227 (2012) 272–279, https://doi.org/10.1524/zkri.2012.1493.

[39] M. Coduri, M. Scavini, M. Brunelli, P. Masala, In situ pair distribution function study on lanthanum doped ceria, Phys. Chem. Chem. Phys. 15 (2013) 8495, https://doi.org/10.1039/c3cp44300k.

[40] C.L. Farrow, P. Juhas, J.W. Liu, D. Bryndin, E.S. Božin, J. Bloch, T. Proffen, S.J. L. Billinge, PDFfit2 and PDFgui: computer programs for studying nanostructure in crystals, J. Phys. 19 (2007), 335219, https://doi.org/10.1088/0953-8984/19/33/335219.

[41] R. Parsons, Handbook of Electrochemical Constants, Butterworths Scientific Publication, London, 1959.

[42] R. Zhou, Y. Zheng, M. Jaroniec, S.-Z. Qiao, Determination of the electron transfer number for the oxygen reduction reaction: from theory to experiment, ACS Catal 6 (2016) 4720–4728, https://doi.org/10.1021/acscatal.6b01581.

[43] U.A. Paulus, T.J. Schmidt, H.A. Gasteiger, R.J. Behm, Oxygen reduction on a high-surface area Pt/Vulcan carbon catalyst: a thin-film rotating ring-disk electrode study, J. Electroanal. Chem. 495 (2001) 134–145, https://doi.org/10.1016/S0022-0728(00)00407-1.

[44] M. Thommes, K. Kaneko, A.v. Neimark, J.P. Olivier, F. Rodriguez-Reinoso, J. Rouquerol, K.S.W. Sing, Physisorption of gases, with special reference to the evaluation of surface area and pore size distribution (IUPAC Technical Report), Pure Appl. Chem. 87 (2015) 1051–1069, https://doi.org/10.1515/pac-2014-1117.

[45] S. Marzorati, M. Longhi, Templating induced behavior of platinum-free carbons for oxygen reduction reaction, J. Electroanal. Chem. 775 (2016) 350–355, https://doi.org/10.1016/j.jelechem.2016.06.032.

[46] M. Thommes, Physical adsorption characterization of nanoporous materials, Chemie Ingenieur Technik 82 (2010) 1059–1073, https://doi.org/10.1002/cite.201000064.

[47] A. Rimola, M. Sodupe, P. Ugliengo, Affinity scale for the interaction of amino acids with silica surfaces, J. Phys. Chem. C 113 (2009) 5741–5750, https://doi.org/10.1021/jp811193f.

[48] K. Artyushkova, Misconceptions in interpretation of nitrogen chemistry from x-ray photoelectron spectra, J. Vacuum Sci. Technol. A 38 (2020), 031002, https://doi.org/10.1116/1.5135923.

[49] K. Artyushkova, A. Serov, S. Rojas-Carbonell, P. Atanassov, Chemistry of multitudinous active sites for oxygen reduction reaction in transition metal-nitrogen-carbon electrocatalysts, J. Phys. Chem. C 119 (2015) 25917–25928, https://doi.org/10.1021/acs.jpcc.5b07653.

[50] J. Lahaye, G. Nansé, A. Bagreev, V. Strelko, Porous structure and surface chemistry of nitrogen containing carbons from polymers, Carbon N Y 37 (1999) 585–590, https://doi.org/10.1016/S0008-6223(98)00225-5.

[51] H.-C. Huang, Y.-C. Lin, S.-T. Chang, C.-C. Liu, K.-C. Wang, H.-P. Jhong, J.-F. Lee, C.-H. Wang, Effect of a sulfur and nitrogen dual-doped Fe–N–S electrocatalyst for the oxygen reduction reaction, J. Mater. Chem. A Mater. 5 (2017) 19790–19799, https://doi.org/10.1039/C7TA05030E.

[52] R. Li, F. Liu, Y. Zhang, M. Guo, D. Liu, Nitrogen, sulfur Co-doped hierarchically porous carbon as a metal-free electrocatalyst for oxygen reduction and carbon dioxide reduction reaction, ACS Appl. Mater. Interfaces. 12 (2020) 44578–44587, https://doi.org/10.1021/acsami.0c06506.

[53] X. Zhao, Q. Zhang, C.-M. Chen, B. Zhang, S. Reiche, A. Wang, T. Zhang, R. Schlögl, D. Sheng Su, Aromatic sulfide, sulfoxide, and sulfone mediated mesoporous carbon monolith for use in supercapacitor, Nano Energy 1 (2012) 624–630, https://doi.org/10.1016/j.nanoen.2012.04.003.

[54] X. Wang, J. Wang, D. Wang, S. Dou, Z. Ma, J. Wu, L. Tao, A. Shen, C. Ouyang, Q. Liu, S. Wang, One-pot synthesis of nitrogen and sulfur co-doped graphene as efficient metal-free electrocatalysts for the oxygen reduction reaction, Chem. Commun. 50 (2014) 4839–4842, https://doi.org/10.1039/c4cc00440j.

[55] Y. Cheng, Y. Wang, Q. Wang, Z. Liao, N. Zhang, Y. Guo, Z. Xiang, Hierarchically porous metal-free carbon with record high mass activity for oxygen reduction and Zn-air batteries, J. Mater. Chem. A Mater. 7 (2019) 9831–9836, https://doi.org/10.1039/C9TA02220A.

[56] J. Li, Y. Zhang, X. Zhang, J. Huang, J. Han, Z. Zhang, X. Han, P. Xu, B. Song, N Dual-doped graphene-like carbon nanosheets as efficient oxygen reduction reaction Electrocatalysts, ACS Appl. Mater. Interfaces 9 (2017) 398–405, https://doi.org/10.1021/acsami.6b12547.

[57] C. Fu, L. Luo, L. Yang, S. Shen, G. Wei, J. Zhang, Breaking the scaling relationship of ORR on carbon-based single-atom catalysts through building a local collaborative structure, Catal. Sci. Technol. 11 (2021) 7764–7772, https://doi.org/10.1039/D1CY01195B.

[58] R.W.G. Wychhoff, Crystal Structures, Interscience Publishers, New York, London, Sydney, 1963.

[59] F. Bertaut, La structure de sulfure de fer, J. de Physique et Du Radium 15 (1954) 775.

[60] D.R. Wilburn, W.A. Bassett, Hydrostatic compression of iron and related compounds; an overview, Am. Mineralogist 63 (1978) 591–596.

[61] Z.S. Basinski, W. Hume-Rothery, A.L. Sutton, The lattice expansion of iron, Proc. R. Soc. Lond. A Math. Phys. Sci. 229 (1955) 459–467, https://doi.org/10.1098/rspa.1955.0102.

[62] A. Janosi, La structure du sulfure cuivreux quadratique, Acta Crystallogr. 17 (1964) 311–312, https://doi.org/10.1107/S0365110X64000743.

[63] W.L. Bragg, The crystalline structure of copper, Lond. Edinburgh. Dublin Philos. Mag. J. Sci. 28 (1914) 355–360, https://doi.org/10.1080/14786440908635219.

[64] A.C. Ferrari, J. Robertson, Interpretation of Raman spectra of disordered and amorphous carbon, Phys. Rev. B 61 (2000) 14095–14107, https://doi.org/10.1103/PhysRevB.61.14095.

[65] A. Tagliaferro, M. Rovere, E. Padovano, M. Bartoli, M. Giorcelli, Introducing the novel mixed gaussian-lorentzian lineshape in the analysis of the raman signal of biochar, Nanomaterials 10 (2020) 1748, https://doi.org/10.3390/nano10091748.

[66] K. Bogdanov, A. Fedorov, V. Osipov, T. Enoki, K. Takai, T. Hayashi, V. Ermakov, S. Moshkalev, A. Baranov, Annealing-induced structural changes of carbon onions: high-resolution transmission electron microscopy and Raman studies, Carbon N Y 73 (2014) 78–86, https://doi.org/10.1016/j.carbon.2014.02.041.

[67] C. Greco, U. Cosentino, D. Pitea, G. Moro, S. Santangelo, S. Patanè, M. D'Arienzo, M. Fiore, F. Morazzoni, R. Ruffo, Role of the carbon defects in the catalytic oxygen reduction by graphite nanoparticles: a spectromagnetic, electrochemical and

computational integrated approach, Phys. Chem. Chem. Phys. 21 (2019) 6021–6032, https://doi.org/10.1039/C8CP07023G.
[68] Y. Belaustegui, F. Pantò, L. Urbina, M.A. Corcuera, A. Eceiza, A. Palella, C. Triolo, S. Santangelo, Bacterial-cellulose-derived carbonaceous electrode materials for water desalination via capacitive method: the crucial role of defect sites, Desalination 492 (2020), 114596, https://doi.org/10.1016/j.desal.2020.114596.
[69] F. Tuinstra, J.L. Koenig, Raman spectrum of graphite, J. Chem. Phys. 53 (1970) 1126–1130, https://doi.org/10.1063/1.1674108.
[70] S. Santangelo, M. Lanza, C. Milone, Evaluation of the overall crystalline quality of amorphous carbon containing multiwalled nanotubes, J. Phys. Chem. C 117 (2013) 4815–4823, https://doi.org/10.1021/jp310014w.
[71] D. Jiang, B.G. Sumpter, S. Dai, Unique chemical reactivity of a graphene nanoribbon's zigzag edge, J. Chem. Phys. 126 (2007), 134701, https://doi.org/10.1063/1.2715558.
[72] Z. Xu, X. Fan, H. Li, H. Fu, W.M. Lau, X. Zhao, Edges of graphene and carbon nanotubes with high catalytic performance for the oxygen reduction reaction, Phys. Chem. Chem. Phys. 19 (2017) 21003–21011, https://doi.org/10.1039/C7CP03416D.
[73] S. Łoś, L. Duclaux, W. Kempiński, M. Połomska, Size effect in the characterization of microporous activated nanostructured carbon, Microporous Mesoporous Mater. 130 (2010) 21–25, https://doi.org/10.1016/j.micromeso.2009.10.007.
[74] Y. Cao, Z. Liu, Y. Tang, C. Huang, Z. Wang, F. Liu, Y. Wen, B. Shan, R. Chen, Vaporized-salt-induced sp3-hybridized defects on nitrogen-doped carbon surface towards oxygen reduction reaction, Carbon N Y 180 (2021) 1–9, https://doi.org/10.1016/j.carbon.2021.04.059.
[75] Y. Lin, X. Sun, D.S. Su, G. Centi, S. Perathoner, Catalysis by hybrid sp^2 /sp^3 nanodiamonds and their role in the design of advanced nanocarbon materials, Chem. Soc. Rev. 47 (2018) 8438–8473, https://doi.org/10.1039/C8CS00684A.
[76] S. Santangelo, C. Milone, Do nanotubes follow an amorphization trajectory as other nanocarbons do? J. Phys. Chem. C 117 (2013) 14206–14212, https://doi.org/10.1021/jp4038599.
[77] P.G. Collins, Defects and Disorder in Carbon Nanotubes, Oxford University Press, 2017. 10.1093/oxfordhb/9780199533053.013.2.
[78] J. Zhang, J. Zhang, F. He, Y. Chen, J. Zhu, D. Wang, S. Mu, H.Y. Yang, Defect and doping Co-engineered non-metal nanocarbon ORR Electrocatalyst, Nanomicro Lett 13 (2021) 65, https://doi.org/10.1007/s40820-020-00579-y.
[79] I. Galbiati, C.L. Bianchi, M. Longhi, A. Carrà, L. Formaro, Iron and copper containing oxygen reduction catalysts from templated glucose-histidine, Fuel Cells (2010) 251–258, https://doi.org/10.1002/fuce.200900142.
[80] A.B. Suriani, N.A. Asli, M. Salina, M.H. Mamat, A.A. Aziz, A.N. Falina, M. Maryam, M.S. Shamsudin, R. Md Nor, S. Abdullah, M. Rusop, Effect of iron and cobalt catalysts on the growth of carbon nanotubes from palm oil precursor, IOP Conf. Ser. Mater. Sci. Eng 46 (2013), 012014, https://doi.org/10.1088/1757-899X/46/1/012014.
[81] H. Yoshida, S. Takeda, T. Uchiyama, H. Kohno, Y. Homma, Atomic-scale in-situ observation of carbon nanotube growth from solid state iron carbide nanoparticles, Nano Lett. 8 (2008) 2082–2086, https://doi.org/10.1021/nl080452q.
[82] Z. He, J.-L. Maurice, A. Gohier, C.S. Lee, D. Pribat, C.S. Cojocaru, Iron catalysts for the growth of carbon nanofibers: fe, Fe_3C or both? Chem. Mater. 23 (2011) 5379–5387, https://doi.org/10.1021/cm202315j.